

Wide field CCD photometry of the globular cluster M92

Kang Hwan Lee

Astronomy Program, SEES, Seoul National University, Seoul 151-742, Korea

khlee@astro.snu.ac.kr

Hyung Mok Lee

Astronomy Program, SEES, Seoul National University, Seoul 151-742, Korea

hmlee@astro.snu.ac.kr

Gregory G. Fahlman

Canada-France-Hawaii Telescope Cooperation, Hawaii 96743, USA

fahlman@cfht.hawaii.edu

and

Myung Gyoon Lee

Astronomy Program, SEES, Seoul National University, Seoul 151-742, Korea

mglee@astrog.snu.ac.kr

Received _____; accepted _____

ABSTRACT

We present wide field CCD photometry of a galactic globular cluster M92 obtained in the V and I bands with the CFH12K mosaic CCD at the Canada-France-Hawaii Telescope. A well-defined color-magnitude diagram is derived down to 5 magnitudes fainter than the cluster main sequence turn-off. After removing the background contribution, we obtain luminosity and mass functions, surface density profiles, and the surface number density maps of the stars belonging to the cluster. The surface density profile of all stars shows that the cluster’s halo extends at least out to $\sim 30'$ from the cluster center in agreement with previous study, but the profile of faint stars at the very outer region of the cluster shows a different gradient compared with that of bright stars. For a mass function of the form $\Phi(M) \propto M^{-(1+x)}$, we find that the inner region ($5' < r < 9'$) of the cluster has $x \simeq 1.2 \pm 0.2$, whereas the outer region ($9' < r < 15'$) has $x \simeq 1.8 \pm 0.3$, clearly indicating a mass segregation of the cluster. An estimate of the photometric mass of the cluster implies that the remnant populations (white dwarfs and neutron stars) contribute at least 25% of the total cluster mass. The surface density map of M92 shows some evidence that the tidal tail of M92 may be oriented perpendicular to the direction toward the Galactic center.

Subject headings: Galaxy: globular clusters: individual (M92) - Galaxy: kinematics and dynamics - stars: luminosity function, mass function

1. INTRODUCTION

Globular clusters are good laboratories for testing theories of stellar dynamics and galactic structure. All globular clusters ultimately decay, through a combination of internal

(two body relaxation, and stellar evolution) and external (gravitational shocks due to the Galactic bulge and disk, and dynamical friction) processes (Aguilar, Hut, & Ostriker 1988). Lee & Goodman (1995) and Gnedin & Ostriker (1997) predicted that possibly as many as half of the present-day Galactic globular clusters would be disrupted in another Hubble time. Many previous studies have shown that tidal shocks play a very important role in cluster evolution by accelerating the destruction of the cluster (e.g. Ostriker, Spitzer, & Chevalier 1972; Gnedin & Ostriker 1997; Gnedin, Lee, & Ostriker 1999). Lee & Ostriker (1987) predicted that, for a given tidal field, the outer structure of a globular cluster will be more populated than that of a King model, since the density at the tidal radius would not be exactly zero. In addition, the cluster is expected to have tidal tails because the equipotential surface is not spherical. The presence of tidal tails from globular clusters has begun to be explored only recently because of difficulties in obtaining accurate wide field photometry. The development of computing power and wide field digital detectors now allows us to study these very interesting parts of globular clusters in detail. Indications of tidal tails around globular clusters were found in several previous studies of globular cluster radial density profiles. Grillmair et al. (1995) examined the outer structure of 12 Galactic globular clusters, and found that 10 of their sample clusters showed extra-tidal wings in their surface density profiles. Later, Lehmann & Scholz (1997) reported the discovery of tidal tails in 5 out of 7 globular clusters. Evidence of tidal extensions are even found in four globular clusters in M31 (Grillmair 1996; Holland, Fahlman, & Richer 1997). Leon, Meylan, & Combes (2000) investigated 20 Galactic globular clusters with Schmidt plates and films, and found that all of the clusters that do not suffer from strong observational biases, show tidal tails. On the theoretical side, Combes, Meylan, & Leon (1999) used N-body simulations to show that two giant tidal tails are expected to exist along the galactic orbit of a globular cluster. Yim & Lee (2002) also examined the general evolution of the clusters using N-body simulation and showed that the cluster density profiles appear to become

somewhat shallower just outside the tidal boundary, and that the directions of the tidal tails depend on the location in the Galaxy as well as the cluster orbit.

Recently, Odenkirchen et al. (2001) reported the discovery of two well defined tidal tails emerging from the sparse, remote globular cluster Palomar 5. They used the CCD images from Sloan Digital Sky Survey (SDSS). Except for this study (and those of the clusters in M31), all the previous observational works on globular cluster tidal tails were based on data from photographic plates. However, such data generally are not deep enough to examine the low mass stars which dominate the outer parts of globular clusters, and the photographic photometry tends to show greater scatter than that based on CCD data.

In the specific case of M92, Testa et al. (2000) investigated the dynamical structure using plates from the Digitized Second Palomar Sky Survey (DPOSS). Although they found some evidence for an elongation in the extra-tidal extension from their surface density map, the significance of their result was low. In this paper, we report the results of a similar analysis using deep CCD images. We surveyed a $2^\circ \times 2^\circ$ region centered on M92 with CFH12K in order to study the dynamical structure and tidal tails of the cluster. We also performed a very detailed analysis of the main sequence mass function, which was impossible to do in the study using photographic plates.

M92 (NGC 6341) is a very metal poor ($[\text{Fe}/\text{H}] = -2.24$) globular cluster located at a distance from the galactic center of $R_{GC} = 9.1$ kpc, and is $Z_{GC} = 4.3$ kpc above the galactic plane (Harris 1996).

This paper is organized as follows. Sect. 2 presents the data and the reduction procedures. In Sect. 3, we show CMDs and discuss the blue straggler stars. The radial profiles of stars in different magnitude ranges are obtained in Sect. 4. The resulting LFs and MFs are presented and discussed in Sect. 5, and the photometric mass is estimated in Sect. 6. In Sect. 7, the surface density maps are discussed. Final results are summarized in

Sect. 8.

2. OBSERVATION AND DATA REDUCTION

The observations were made with the 3.6 m Canada-France-Hawaii Telescope (CFHT) during 2000 June 27-29, using CFH12K, a 6×2 mosaic of 2048×4096 CCDs. The instrument has an angular scale of $0.''206/\text{pixel}$ at the $f/4$ prime focus of the CFHT, giving a field of view of $42' \times 28'$. The CFH12K camera is well suited for this study as it covers a large area on the sky with well sampled images. A total of 10 fields through V and I filters were observed covering a field of $120' \times 120'$, significantly larger than the tidal radius of M92, $15.''2$, estimated by Trager et al. (1995). The positions of the observed fields relative to the center of M92 are shown in Fig. 1, and pertinent observational information is given in Table 1. All of the science images were obtained under good seeing conditions (FWHM of $\sim 0.''8$). We also obtained frames of fields containing Landolt (1992) standard stars for photometric calibration, and several twilight (flat-field), bias and dark frames were also taken to permit removal of the instrument signature from the science data.

EDITOR: PLACE FIGURE 1 HERE.

EDITOR: PLACE TABLE 1 HERE.

All pre-processing, bias and dark subtraction and flat fielding, was performed using the FITS Large Images Processing software (FLIPS), a very efficient package developed by Jean-Charles Cuillandre for the reduction of CCD mosaic images (see Kalirai et al. 2001 for more information). Instrumental magnitudes of the point sources in the images were derived using the programs DAOPHOT II/ALLSTAR (Stetson 1994). The point-spread

function (PSF) is different for each of the 12 CCDs on the mosaic, so the analysis is done separately for each chip. In those cases where we have 3 images in the same band (F3, F4, F5, F6 and F7 in V), we averaged them using the ALIGN and IMCOMBRED commands within FLIPS. For the other fields, we analyzed each image separately and then averaged the photometry to get mean instrumental magnitudes. We used the stellarity index of SExtractor (Bertin & Arnouts 1996) for separating stars from background galaxies and, as an example, Fig. 2 shows this parameter for sources detected in F3. Those objects with a stellarity index greater than 0.8 were considered to be stars. This process has excluded most of the background galaxies. After further cuts, based on the two DAOPHOT parameters, the magnitude error (< 0.2) and the PSF fitting parameter, χ^2 (< 2), were made to eliminate spurious measurements, the data sets in each filter were matched and the positions, instrumental magnitudes, and colors were obtained for all the stars.

EDITOR: PLACE FIGURE 2 HERE.

The instrumental magnitudes were then transformed to the standard Johnson-Cousins photometric system by using the photometric standard stars in SA113 (Landolt 1992). The standard values for the color term and the atmospheric extinction coefficient given on the CFHT home page were used to find the zero points of each chip separately. The instrumental zero points for the chips were almost identical (within a range of 0.1 mag) because FLIPS normalizes the background sky value to the chip with the highest sky value (lowest gain). Fig. 3 shows the differences between our photometry of the Landolt (1992) standard stars and the standard values.

EDITOR: PLACE FIGURE 3 HERE.

3. The COLOR-MAGNITUDE DIAGRAM

The derived CMD for the central region of the cluster is shown in Fig. 4. and is based on the data obtained by merging the long and short exposure data. The short exposure data were used to cover the center ($r < 2'$) of the cluster where bright stars were totally saturated in long exposure data, and to show the evolved sequences of the cluster. The inner core of the cluster ($r < 1'$) is too crowded to resolve stars even in short exposure data. The solid line is a fiducial line from the previous study by Harris et al. (1997), showing a good agreement between the two. Our primary concern is the properties of the cluster main sequence stars, so we will deal with mainly this part of the CMD in the following.

The CMD of the distant fields was used for first-step of removing background/foreground field contamination. For comparison we show CMDs of inner ($2' < r < 15'$) and outer ($r > 45'$) regions separately in Fig. 5. We selected stars within the illustrated color band ($\Delta(V - I) = 0.5$) centered on the fiducial magnitude as candidate main sequence stars. Our selection criteria is wide enough to include all members of cluster main sequence but it will also include some contribution from field stars that can only be removed statistically.

Twelve stars in the box of Fig. 4 are thought to be blue straggler (BS) stars. BS stars are known to be more centrally concentrated than others in globular clusters (Bailyn 1995). In Fig. 6, we compared the radial distribution of BS stars with that of subgiant branch (SGB) star. Though the sample of BS stars is very small, we find no evidence that the BS stars are more concentrated than SGB stars. But further discussions on the BS stars are beyond the scope of this study.

EDITOR: PLACE FIGURE 4 HERE.

EDITOR: PLACE FIGURE 5 HERE.

EDITOR: PLACE FIGURE 6 HERE.

4. THE RADIAL DENSITY PROFILE

4.1. Incompleteness Correction

The stars within the specified range in the CM diagram are likely to be members of the cluster. However, because of crowding effect, we cannot recover all the members of cluster. In order to study the spatial distribution of stars, we need to correct for the crowding. This is called incompleteness correction. Usually, the completeness depends on the level of crowding which depends on location with respect to the cluster center. An increasing contribution of the sky background also reduces the detection probability for faint stars. To correct for incompleteness, we ran artificial star tests on the V frames, using DAOPHOT/ADDSTAR. We chose 22 chips in four directions from the cluster center. The tests were applied on each chip separately. First, we added artificial stars in each 0.5 mag bin randomly on original images. The number of added stars was designed not to exceed 10% of the total number of stars that is actually present in that bin so as not to enhance original crowding. The new frames obtained in this way were then reduced in an identical manner used on the original frame. In Fig. 7, we showed the plots of the differences between input and output magnitudes for recovered artificial stars selected by the same criteria which were applied to original image reduction. The stars, which have magnitude differences smaller than 0.3 mag are considered as recovered stars. We repeated these procedures 10 times on each chip to obtain meaningful statistics in each magnitude bin. Finally, the incompleteness correction factor f is obtained by $f = n_{rec}/n_{add}$, where n_{add} is the number of added stars and n_{rec} is the number of recovered stars. The resulting incompleteness correction factors applied to correct luminosity functions are listed in Table 2.

EDITOR: PLACE FIGURE 7 HERE.

EDITOR: PLACE TABLE 2 HERE.

4.2. Field Subtraction

Although we have used CMD selection to reduce background/foreground field contribution, there are still many field stars within the defined main sequence band on the CMD (Fig. 5). To build accurate radial density profiles and luminosity functions of the cluster, this contamination needs to be statistically removed. Since the length of tidal tails is an order of 5 tidal radii, or greater (Combes et al. 1999), which is larger than the region surveyed here, a determination of the field density using all the outermost regions could lead to an overestimate. Therefore, in order to estimate the background level as a first step, we selected those regions showing no overdensities in the outermost parts in each magnitude bins after constructing the surface density maps (see section 6 for details). The stellar densities in the selected regions were then averaged with weighting factors proportional to the area of the selected regions. The determined background densities are $0.18 \pm 0.03 \text{ arcmin}^{-2}$ for $18.5 < V < 20.5$, $0.40 \pm 0.04 \text{ arcmin}^{-2}$ for $22 < V < 23.5$, and $0.85 \pm 0.05 \text{ arcmin}^{-2}$ for $18.5 < V < 23.5$.

4.3. Radial Density Profile

The cluster’s radial density profile was obtained by counting all the main sequence stars in annuli with widths of $2 \sim 3$ arcminutes. These numbers were then corrected for field contamination and incompleteness as described in previous sections. The final surface

density of i the annulus was then derived, using:

$$SDP_i = -2.5 \times \log(N_{i,i+1}/A_{i,i+1}) + 2.5 \times \log f + C,$$

where $N_{i,i+1}$ indicates the background subtracted number of stars in the annulus between r_i and r_{i+1} , $A_{i,i+1}$ the area of the annulus and f the incompleteness correction factor.

The constant, C , was chosen to match the profile with that of Trager et al. (1995) in the overlapping region. The effective radius of each annulus is given by:

$$r_i^{eff} = \sqrt{\frac{1}{2} \times (r_i^2 + r_{i+1}^2)}.$$

The final radial density profile of M 92 using the entire main sequence sample of stars ($18.5 < V < 23.5$) is shown in Fig. 8. In the central region ($r < 2'$), the short exposure data were used with smaller radial steps (10 arcseconds). However, the points for the inner most region ($r < 1'$), where the stars are not resolved, were obtained not by counting stars but by surface photometry of the short exposure data. The flux measurements from surface photometry were shifted to match with star counts. These points are shifted to match with the results from outer region. The measured surface density profile is listed in Table 3. In Fig. 8 we see that our result agrees very well with that of Trager et al. (1995). The best fitting single-mass isotropic King model profile is shown on Fig. 8 as a solid line ($W_0 = 8$, $c = 1.85$). The tidal radius of the best-fit King model is $r_t = 840''$, which lies between the $r_t = 740''$ by Testa et al. (2000), and $r_t = 912''$ of Trager et al. (1995). The data exhibits a noticeable deviation from the King model in the outer region. This is a sign of the presence of extra-tidal material.

EDITOR: PLACE FIGURE 8 HERE.

EDITOR: PLACE TABLE 3 HERE.

Grillmair et al. (1995) examined the density profiles of 12 Galactic globular clusters and found that most of them had extra-tidal stars. They described the radial distribution of extra-tidal stars by a power law $\Sigma(r) \propto r^\gamma$ with $-5 < \gamma < -1.6$. Using numerical simulations, Johnston, Sigurdsson, & Hernquist (1999) showed that the extra-tidal population is expected to have $\Sigma(r) \propto r^{-1}$, and that there should be a break in the slope of the surface density profile due to stars being stripped from the cluster. On the other hand, Combes et al. (1999) deduced a slope around $\gamma = -4$ from their N-body simulations. They explain the shallower slope in the observations as the contamination of background-foreground populations. Combes et al. (1999) also predicted that the escaped stars would not be distributed homogeneously within the tails, but form clumps that mark the occurrence of the strongest gravitational shocks. Leon et al. (2000) investigated tidal tails of 20 Galactic globular clusters and computed the slopes of surface density of extra-tidal stars for their sample. The values are in the range of previous studies $-5.03 < \gamma < -0.35$, but not all clusters showed a break in the slope.

Testa et al. (2000) obtained the surface density profile of M 92 using plates from the Digitized Second Palomar Sky Survey. They fitted the extra-tidal profile of the cluster to a power law and found $\gamma = -0.85 \pm 0.08$. From our surface density profile, shown in Fig. 9, we derive $\gamma = -0.82 \pm 0.10$ using only the bright stars ($18.5 < V < 20.5$), which we take to correspond with the stars in the study by Testa et al. (2000). Using the faint stars ($22 < V < 23.5$), we find a steeper slope of $\gamma = -1.31 \pm 0.09$, which is significantly different from that of the bright stars. Using the entire range of calibrated stars ($18.5 < V < 23.5$), we find $\gamma = -1.27 \pm 0.08$. We see a clear clump in the extra-tidal profile (around $r = 2100''$), a feature similar to those predicted by Combes et al. (1999).

It is noteworthy that the slopes of the density profiles for stars in different magnitude bins, have different values in the outer part of the cluster. Since the tidal tails of globular

clusters are preferentially formed by the lowest mass stars (Combes et al. 1999), it is difficult to study tidal tails of globular clusters using only bright stars. This implies that the study of globular clusters tidal tail should be performed using stars with the lowest possible mass that is detectable. It is possible that the difference in slopes of the density profiles in different magnitude bins is a real feature of the cluster. Deep CCD studies of other nearby clusters are needed to verify whether the mass dependence of the density profile slope is a common phenomenon.

EDITOR: PLACE FIGURE 9 HERE.

5. THE LUMINOSITY AND MASS FUNCTION

A luminosity function (LF) was constructed by using the main sequence stars within the cluster’s tidal radius. To investigate any spatial difference, the LFs for an inner region ($5' < r < 9'$) and an outer region ($9' < r < 15'$) was constructed separately. The region of $r < 5'$ was excluded here to avoid the uncertainty due to central crowding. As noted below, HST results are available for the region inside $r < 5'$. To build correct LFs, we applied background subtraction and incompleteness corrections as described in the previous sections. The corrected number of stars in each magnitude bin and the incompleteness factors are given in Table 2, and the results are plotted in Fig. 10. The histogram in Fig. 10 is the LF for all stars within $5' < r < 15'$. We find that the outer LF is steeper than the inner LF, a clear sign of mass segregation in the cluster. The solid line overlaid on the inner LF is the LF of M92 for $r \sim 5'$ derived from HST WFPC2 data by Piotto, Cool, & King (1997). Our result agrees very well with HST result.

The LFs were converted into mass functions (MFs) using the mass-luminosity relation of Baraffe et al. (1997) and a distance modulus of $(m - M)_V = 14.82$ (Gratton et al. 1997).

The calculated MFs are shown in Fig. 11. Representing the MF by a power law,

$$\Phi(M)dM \propto M^{-(1+x)}dM,$$

we derive slopes of $x = 1.2 \pm 0.3$ and $x = 1.8 \pm 0.5$ for the mass range $0.35M_{\odot} < M < 0.8M_{\odot}$ in the inner ($5' < r < 9'$) and outer ($9' < r < 15'$) regions, respectively. The slope for the entire region between $5' < r < 15'$ is $x = 1.3 \pm 0.2$. For the mass range $0.26M_{\odot} < M < 0.73M_{\odot}$, Andreuzzi et al. (2000) derived a slope of $x = 0.71$ between $2' < r < 5'$ from HST data. From these results, we conclude that the slope of the MF increases with distance from the cluster center, as expected from mass segregation in clusters.

McClure et al. (1986) suggested that the slope of MF is related to the metallicity of cluster. Djorgovski, Piotto, & Capaccioli (1993) demonstrated that the MF slopes are determined not only by the metallicity but also by the location in the Galaxy. The strongest dependence is on the Galactocentric distance (R_{GC}): clusters closer to the Galactic center have flatter MFs. At a given Galactocentric distance, clusters with a smaller distance from the Galactic plane (Z_{GC}) have flatter MFs, and at a given position, clusters with lower metallicity have steeper MFs. Capaccioli, Piotto, & Stiavelli (1993) interpreted the dependence on position as the effect of tidal shocks. Disk and bulge shocking act preferentially on stars located in the outer region of the cluster and lead to a loss of low mass stars. As a result the clusters near the Galactic plane, tend to have flatter MFs. Consequently, the relatively steep MF slope of M92 could be explained by its low metallicity ($[\text{Fe}/\text{H}] = -2.24$) and large R_{GC} (9.1 kpc) and Z_{GC} (4.3 kpc).

Piotto et al. (1997) confirmed the relation between Galactocentric positions and MF slopes of globular clusters by comparing LFs of four metal poor globular clusters. They showed that three of four clusters (M15, M30, and M92) have nearly identical LFs, whereas NGC 6397, with the smallest R_{GC} and Z_{GC} , has a distinctly different LF, especially the

fainter part. They suggest that the three globular clusters, which have similar LFs, were formed with similar MFs that have changed little (or changed in similar ways), while NGC 6397 was more vulnerable to tidal shocks. Lee, Fahlman, & Richer (1991) showed that the slope of the cluster mass function can change rapidly only during the final stage of dynamical evolution and that one signature of highly evolved clusters is a significant flattening of the mass function (see also Lee & Goodman 1995, and Takahashi & Lee 2000). The relatively steep MF slope of M92, especially in the outer part of the cluster, suggests that this cluster, although it has experienced substantial mass segregation, has been little affected by tidal shocks.

EDITOR: PLACE FIGURE 10 HERE.

EDITOR: PLACE FIGURE 11 HERE.

6. MASS ESTIMATION

Since we have found nearly all the stars in the cluster outside of the central region with masses greater than $0.35M_{\odot}$, we can estimate the total luminous mass of the cluster by combining our data with that in the HST archive for the cluster center. HST archival data covering $r < 5'$ was obtained and analyzed using HSTphot (Dolphin, 2000). We counted stars within annuli of width $14''$. Since the HST archive data do not cover a full 360 degree azimuthal annulus, we complete the counts by assuming that the cluster has circular symmetry. All the star counts are corrected for completeness and converted to masses using the mass-luminosity relation of Baraffe et al. (1997). The limiting magnitude, defined to be the value where the completeness fraction drops below 50%, and the calculated mass above

the limiting magnitude is listed in Table 4 for each annulus. Summing these estimates, we find that the measured luminous mass is $\sim 7.4 \times 10^4 M_\odot$. This value is clearly only a lower limit to the luminous stellar mass of the cluster. The total mass of the fainter, uncounted stars must be estimated in some way.

We can estimate the total mass of the low mass stars by extrapolating the observed mass functions to the hydrogen burning limit, here taken to be $0.08 M_\odot$. Explicitly, we assume that the observed MF slope applies right to this limit. This may not be an unreasonable assumption because recently, Richer et al. (2002) found that the mass function of the nearby globular cluster M4, which rises slowly toward their lowest observed mass of $0.09 M_\odot$, shows no convincing evidence of a turnover. In any case, the lowest mass stars ($< 0.09 M_\odot$) contribute only small part of the cluster’s total mass (below 5%) even at the steepest slope ($x = 1.8$). The extrapolated mass (that below the limiting magnitude) in each annulus is shown in Table 4. The last column in Table 4 lists the slope of the mass function that was used to calculate the extrapolated mass. These values are based on the results of Andreuzzi et al. (2000) for the region $r < 5'$ and present study for the region $5' < r < 15'$. As expected, the correction for uncounted stars is substantial within the inner arcminute of the cluster. The estimated total mass is $\sim 1.6 \times 10^5 M_\odot$. This value is arguably an upper limit to the total main-sequence mass for two reasons. First, the mass function may not be constant to the limit of $0.08 M_\odot$, and second the MF slope in the core of the cluster ($r < 1'$) is expected to be smaller than the value we used, which was derived from a somewhat more distant region. The luminous mass we determine is smaller than the estimated dynamical mass of $\sim 2.1 \times 10^5 M_\odot$ by Pryor & Meylan 1993. The mass deficiency is probably due entirely to a remnant population in the cluster - white dwarfs and neutron stars. Our derivation of the luminous mass gives an uncertain result for the reasons discussed above and also because it depends on stellar models. The current theoretical models for low temperature stars of low metallicity do not fit the lower main-sequence very

well, leading to another source of systematic uncertainty. With these caveats, we cautiously predict that the remnant population contributes at least 25% to the total mass of M92.

7. SURFACE DENSITY MAP

In order to characterize the distribution of the extra-tidal stars, we constructed surface number density maps as follows. The number counts of main-sequence stars in the surveyed region were binned on a grid of $0.'5 \times 0.'5$. We then convolved the map with a Gaussian kernel of width $2.'5$. The resulting smoothed surface density maps are shown in Fig. 12. The two maps are constructed using: (a) bright stars (about 2 magnitudes below the main-sequence turn-off), and (b) the entire set of stars, which is dominated by faint objects. We overlaid contour levels and marked the tidal radius with a thick circle. The long arrow indicates the direction to the galactic center and the short arrow shows the proper motion ($\mu_\alpha \cos \delta = -3.30 \pm 0.55 \text{ mas yr}^{-1}$, $\mu_\delta = -0.33 \pm 0.70 \text{ mas yr}^{-1}$) compiled by Dinescu, Girard, & van Altena (1999).

From an inspection of the two maps, we see that the shape of the tidal halo is different between the bright and faint stars. In particular, a clump to the SE of the cluster appears in the bright star density map (it also appears in the Fig. 6 of Testa et al. 2000) is not seen in the map for faint stars. It is difficult to see an elongation of the tidal halo with the bright stars only because their number counts are typically too small. Deep CCD photometry is needed to define the shape of the tidal halo, especially for the halo clusters that is expected to have a weak extra-tidal extension.

From Fig. 12, we see a marginal elongation orthogonal to the direction to the Galactic center (NE to SW). Several models (Murali & Dubinski 1999; Combes et al. 1999; Yim & Lee 2002) predict that there may exist two giant tidal tails around the globular cluster.

Combes et al. (1999) showed that the tidal tail follows the cluster orbit, but Yim & Lee (2002) showed that the directions of the tidal tails depend on the location in the Galaxy as well as the cluster orbit. Tidal tails have been detected around many globular clusters (Grillmair et al. 1995; Leon et al. 2000; Odenkirchen et al. 2001) and some dwarf spheroidal galaxies of the Local Group (Mateo, Olszewski, & Morrison 1998). Possible explanations of the weak tidal halo of M92 are that the tail may be compressed along the line of sight or the evaporating stars might not yet have been formed a tidal stream. According to the numerical simulation by Yim & Lee (2002), tidal tail is longest near the apogee and shortest near the perigee. Therefore M92 might be near perigee.

EDITOR: PLACE FIGURE 12 HERE.

8. SUMMARY

We have carried out a wide field CCD survey of M92 and investigated the dynamical structure and stellar population of the cluster M92. The main results of our study are:

- (i) We find some candidates of BS stars in the CMD. We can not find any evidence that the BS stars are more centrally concentrated than SGB stars.
- (ii) The radial density profile of M92 reveals the presence of extra tidal material. From the King model fitting method, we derived a tidal radius for M92 of $r_t = 840''$. We find that the extra-tidal density profile is shallower for the bright star when compared to the fainter stars.
- (iii) We show that the slope of cluster MF increases toward the outer part of the cluster, as expected from mass segregation. The relatively steep MF slope of M92, especially in the outer part of the cluster, suggests that this cluster has not been strongly affected by

tidal shocks.

(iv) From an estimation of the photometric mass of M92, we conclude that the maximum value of the cluster’s MS mass is $\sim 1.6 \times 10^5 M_{\odot}$. At least 25% of the total cluster mass may be contributed by the remnant population.

(v) From the surface density map, we see a slight elongation of the cluster halo perpendicular to the direction to the Galactic center. Possible explanations of the weak tidal halo of M92 are that the tidal tail may be compressed along the line of sight, or the evaporating stars may not yet have been formed a tidal stream.

Finally, we note the need for deeper CCD photometry to investigate extra-tidal stars, especially for clusters, like M92, which have weak tidal extensions.

REFERENCES

- Aguilar, L., Hut, P., & Ostriker, J. P. 1988, ApJ, 335, 720
- Andreuzzi, G., Buonanno, R., Fusi Pecci, F., Iannicola, G., & Marconi, G. 2000, A&A, 353, 944
- Bailyn, C. D. 1995, ARA&A, 33, 133
- Baraffe, I., Chabrier, G., Allard, F., & Hauschildt, P. H. 1997, A&A, 327, 1054
- Bertin, E., & Arnouts, S. 1996 A&AS, 117, 393
- Capaccioli, M., Piotto, G., & Stiavelli M., 1993 MNRAS, 261, 819
- Cardelli, J. A., Clayton, G. C., & Mathis, J. S. 1988, ApJ, 329, L33
- Combes, F., Leon, S., & Meylan, G. 1999, A&A, 352, 149
- Djorgovski, S., Piotto, G., & Capaccioli, M. 1993, AJ, 105, 2148
- Dolphin, A. E. 2000, PASP, 112, 1383
- Dinescu, D. I, Girard, T. M., & van Altena W. F. 1999, AJ, 117, 1792
- Fahlman, G. G., Richer, H. B., & Nemec, J. 1991, ApJ, 380, 124
- Gnedin, O. Y., Lee, H. M., & Ostriker, J. P. 1999, ApJ, 522, 935
- Gnedin, O. Y., & Ostriker, J. P. 1997, ApJ, 474, 223
- Gratton, R. G., Fusi Pecci, F., Carretta, E., Clementini, G., Corsi, C. E., & Lattanzi M. 1997, ApJ, 491, 749
- Grillmair, C. J., Freeman, K. C., Irwin, M., & Quinn, P. J. 1995, AJ, 109, 2553

- Grillmair, C. J., et al. 1996, AJ, 111, 2293
- Harris, W. E. 1996, AJ, 112, 1487
- Harris, W. E., et al. 1997, AJ, 114, 1030
- Holland, S., Fahlman, G. G., & Richer, H. B. 1997, AJ, 114, 1488
- Johnston, K. V., Sigurdsson, S., & Hernquist, L. 1999, MNRAS, 302, 771
- Kalirai, J. S., et al. 2001, AJ, 122, 257
- Landolt, A. U. 1992, AJ, 104, 340
- Lee, H. M., Fahlman, G. G., & Richer, H. B. 1991, ApJ, 366, 455
- Lee, H. M., & Goodman, G. 1995, ApJ, 443, 109
- Lee, H. M., & Ostriker, J. P. 1987, ApJ, 322, 123
- Lehmann, I., & Scholz, R. -D. 1997, A&A, 320, 776
- Leon, S., Meylan, G., & Combes, F. 2000, A&A, 359, 907
- Mateo, M., Olszewski, E. W., & Morrison, H. L. 1998, ApJ, 508, L55
- McClure, R. D., et al. 1986, ApJ, 307, L49
- Murali, C., & Dubinski, J. 1999, AJ, 118, 911
- Odenkirchen, M., et al. 2001, ApJ, 548, L165
- Ostriker, J. P., Spitzer, L. Jr., & Chevalier, R. A. 1972, ApJ, 176, L51
- Piotto, G., Cool, A. M., & King, I. R. 1997, AJ, 113, 1345

- Pryor, C., & Meylan, G. 1993, in ASP Conf. Ser.50 Structure and Dynamics of Globular Clusters, ed. S. G. Djorgovski & G. Meylan, 357
- Richer, H. B., et al. 2002, ApJ, 574L, 151
- Stetson, P. B. 1994, PASP, 106, 250
- Takahashi, K. & Lee, H. M. 2000, MNRAS, 316, 671
- Testa, V., Zaggia, S. R., Andreon, G. L., Scaramella, R., Djorgovski, S. G., & de Carvalho R. 2000, A&A, 356, 127
- Trager, S., King, I., Djorgovski, S., & Roden, J. 1995, AJ, 109, 218
- Yim, K. J., & Lee, H. M. 2002, JKAS, 35, 75

Fig. 1.— Location of 10 observed fields, with the origin set on the cluster center. The circle indicates derived tidal radius $r_t = 14'$. Each frame has a field of view of $42' \times 28'$.

Fig. 2.— Stellarity index of objects in F3 region.

Fig. 3.— Differences between our photometry of the Landolt (1992) standards and their published values. The differences ΔV and $\Delta(V - I)$ are (Landolt's - ours).

Fig. 4.— CMD for the central region of the cluster ($1' < r < 8'$). This is the result of merging the long and short exposure data. The solid line is a fiducial line from Harris et al. (1997).

Fig. 5.— CMDs divided by inner ($2' < r < 15'$) and outer ($r > 45'$) region of the cluster. The overlaid lines indicate criteria for selecting cluster MS stars to reduce field star contribution.

Fig. 6.— Cumulative radial distributions for SGB stars and BSS stars.

Fig. 7.— Result of artificial star test for one direction from cluster center. The difference ΔV is $V_{add} - V_{rec}$.

Fig. 8.— Radial density profile of M92 using the entire main sequence stars ($18.5 < V < 23.5$) within CMD criteria. Filled triangles, short exposure data; filled circles, long exposure data; open circles, Trager et al. (1995); solid line, single-mass isotropic King model ($W_0 = 8$, $c = 1.85$).

Fig. 9.— Fit of power laws to the external profile of M92. Triangles, the profile of bright stars ($18.5 < V < 20.5$); filled squares, the profile of faint stars ($22 < V < 23.5$); filled circles, the profile of all stars ($18.5 < V < 23.5$); solid lines are the fitting power laws with $\gamma = -0.82 \pm 0.10$, $\gamma = -1.31 \pm 0.09$, and $\gamma = -1.27 \pm 0.08$.

Fig. 10.— Luminosity functions of inner ($5' < r < 9'$) and outer ($9' < r < 15'$) region for M92. The histogram is a LF of all stars within $5' < r < 15'$. A solid line overlayed with inner LF is the result from Piotto et al. (1997). For convinient comparison, the LFs are arbitrarily shifted.

Fig. 11.— Mass functions corresponding to the normalized luminosity functions of Fig. 10. The lines show the indicated mass spectral index x (see text).

Fig. 12.— Surface density maps and contours of levels of different magnitude ranges ((a) $18.5 < V < 20$, (b) $18.5 < V < 23.5$). The tidal radius is marked as a thick circle. The two arrows indicate the directions of the galacic center (long one) and compiled proper motion (Dinescu et al. 1999).

Table 1. Obsevatinal Information of M92

Field	V-Filter	date	I-Filter	date
F1	2×1200s	Jun. 28 2000	2×900s	Jun. 27 2000
F2	2×1200s	Jun. 28 2000	2×900s	Jun. 27 2000
F3	3×1200s	Jun. 28 2000	2×900s	Jun. 28 2000
F4	3×1200s	Jun. 28 2000	2×900s	Jun. 28 2000
F5	3×1200s	Jun. 28 2000	2×900s	Jun. 29 2000
F6	3×1200s	Jun. 28 2000	2×900s	Jun. 29 2000
F7	3×1200s	Jun. 29 2000	2×900s	Jun. 29 2000
F8	2×1200s	Jun. 29 2000	1×900s	Jun. 29 2000
F9	2×1200s	Jun. 29 2000	2×900s	Jun. 29 2000
F10	2×1200s	Jun. 29 2000	2×900s	Jun. 29 2000
F1	2×20s	Jun. 27 2000	2×20s	Jun. 27 2000
F2	2×20s	Jun. 27 2000	2×20s	Jun. 27 2000

Table 2. Corrected Luminosity Functions and Incompleteness Correction Factors

V	Inner ($5' < r < 9'$)		Outer ($9' < r < 15'$)		Inner + Outer	
	N	f	N	f	N	f
18.25-18.75	168.8	1.0	16.9	1.0	185.7	1.0
18.75-19.25	207.0	1.0	36.4	1.0	243.4	1.0
19.25-19.75	366.5	1.0	79.3	1.0	445.8	1.0
19.75-20.25	557.5	1.0	112.4	1.0	669.9	1.0
20.25-20.75	667.7	1.0	125.1	1.0	792.8	1.0
20.75-21.25	822.0	0.97	172.6	1.0	989.7	0.98
21.25-21.75	863.3	0.96	208.7	0.97	1074.2	0.96
21.75-22.25	978.3	0.92	258.7	0.93	1239.8	0.92
22.25-22.75	1167.2	0.92	278.2	0.92	1448.4	0.92
22.75-23.25	1435.8	0.90	381.9	0.91	1821.9	0.90
23.25-23.75	1999.5	0.79	523.1	0.86	2505.6	0.81
23.75-24.25	3039.0	0.60	728.8	0.67	3556.5	0.65

Table 3. Radial Density Profiles

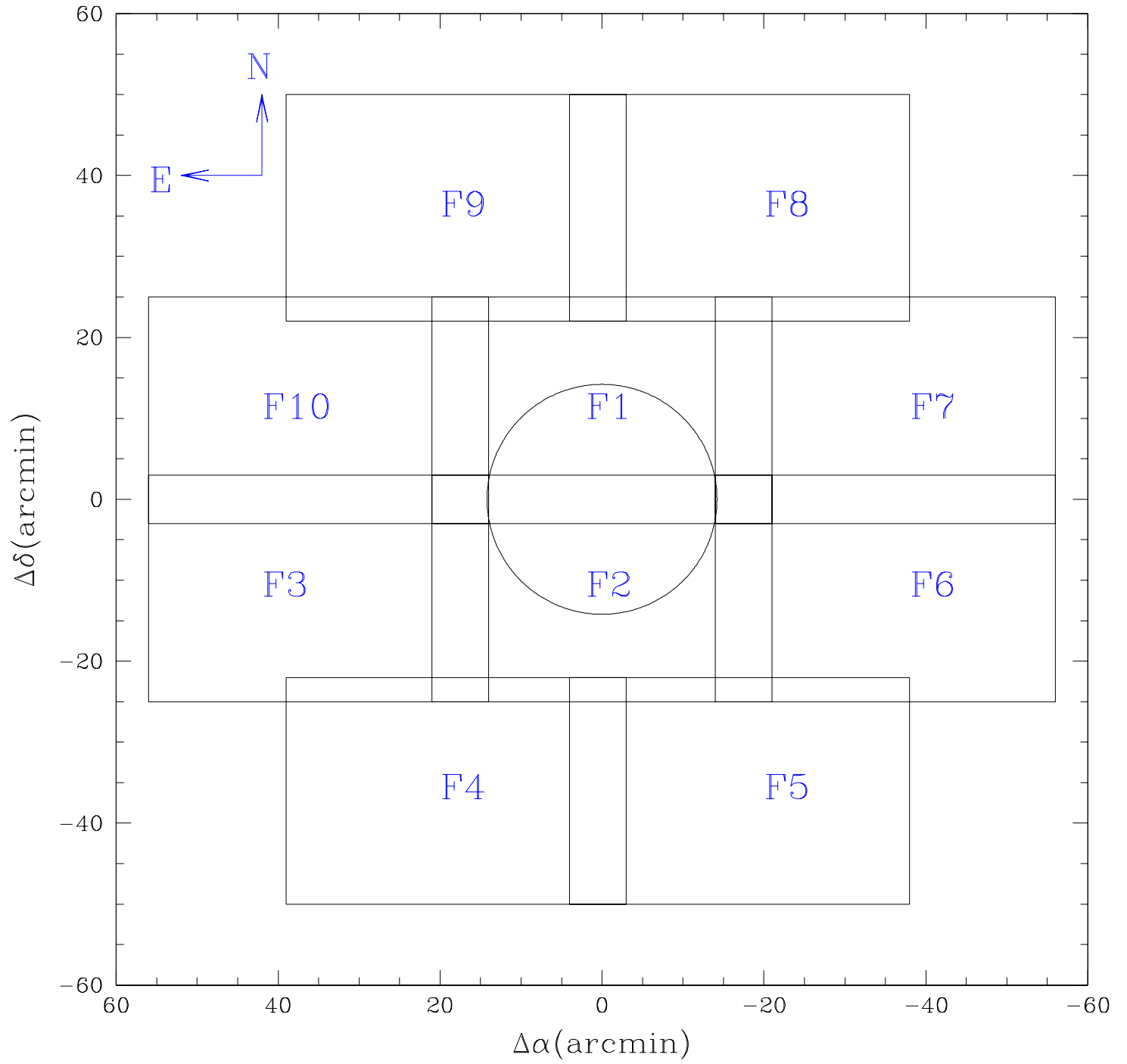
Short Exposure ($15 < V < 20$)				Long Exposure ($18.5 < V < 23.5$)			
$\log r_{eff}$	$\#/\text{arcmin}^2$	SDP	error	$\log r_{eff}$	$\#/\text{arcmin}^2$	SDP	error
(arcsec)		(mag/arcsec ²)		(arcsec)		(mag/arcsec ²)	
0.412	-	15.50	0.14	2.185	714.156	21.17	0.01
0.849	-	15.68	0.14	2.327	428.225	21.72	0.01
1.199	-	16.38	0.10	2.434	208.647	22.50	0.01
1.406	-	17.11	0.12	2.520	116.156	23.14	0.02
1.548	-	17.42	0.12	2.592	57.688	23.90	0.02
1.656	-	18.02	0.15	2.654	29.572	24.62	0.03
1.742	-	18.27	0.15	2.708	17.715	25.18	0.03
1.814	0.268	18.68	0.17	2.756	10.972	25.70	0.04
1.876	0.156	19.27	0.21	2.821	5.431	26.46	0.04
1.930	0.139	19.39	0.21	2.893	2.358	27.37	0.05
1.978	0.116	19.59	0.22	2.955	1.356	27.97	0.06
2.022	0.059	20.32	0.30	3.023	0.699	28.69	0.07
2.061	0.055	20.39	0.38	3.091	0.411	29.26	0.08
2.097	0.058	20.35	0.28	3.160	0.316	29.55	0.07
2.131	0.053	20.43	0.28	3.226	0.187	30.12	0.09
2.162	0.044	20.65	0.30	3.284	0.155	30.33	0.10
2.191	0.047	20.57	0.28	3.335	0.243	29.84	0.07
2.243	0.030	21.07	0.34	3.381	0.190	30.10	0.08

Table 3—Continued

Short Exposure ($15 < V < 20$)				Long Exposure($18.5 < V < 23.5$)			
$\log r_{eff}$	$\#/\text{arcmin}^2$	SDP	error	$\log r_{eff}$	$\#/\text{arcmin}^2$	SDP	error
(arcsec)		(mag/arcsec ²)		(arcsec)		(mag/arcsec ²)	
2.267	0.022	21.37	0.40	3.422	0.155	30.33	0.08
2.290	0.022	21.37	0.40	3.460	0.125	30.56	0.09
2.323	0.011	22.15	0.40	3.512	0.114	30.66	0.08

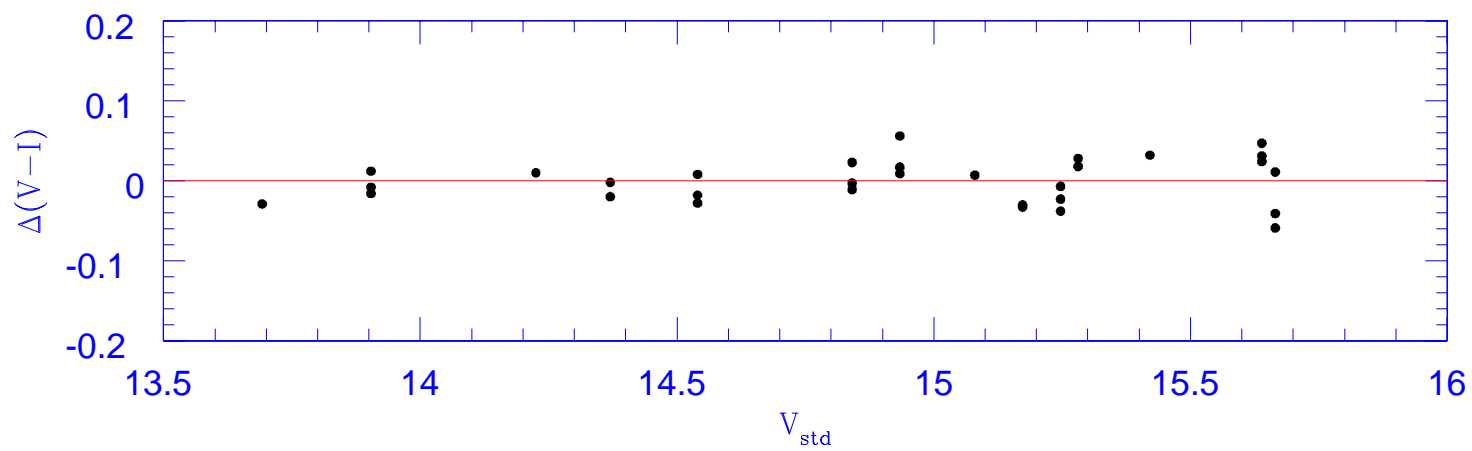
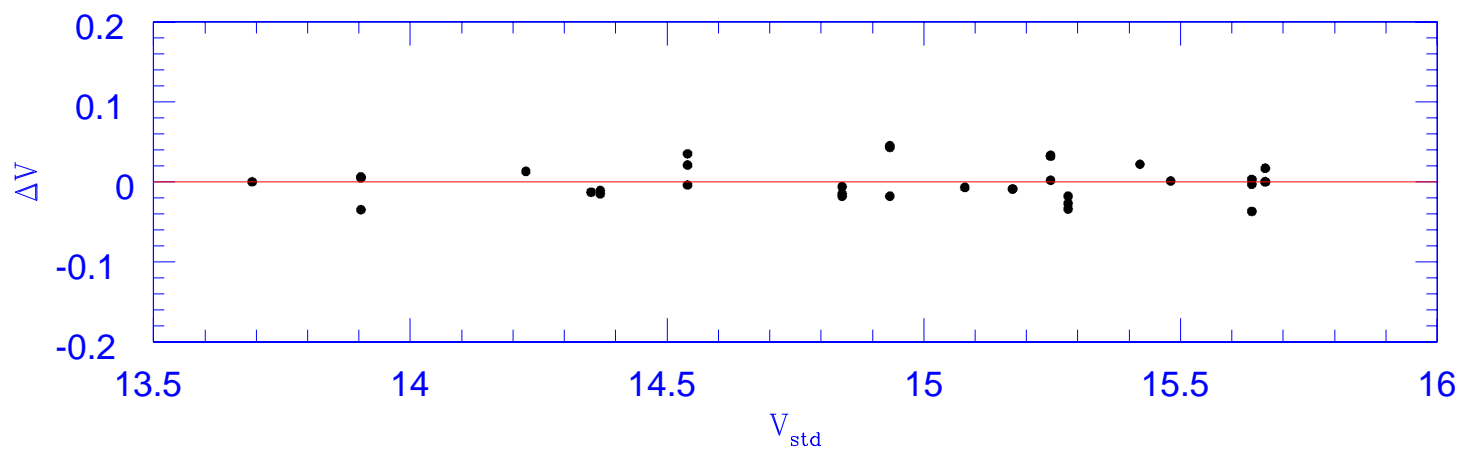
Table 4. Estimated Masses

r''	V_{lim}	mesured (M_{\odot})	extrapolated (M_{\odot})	total (M_{\odot})	slope (x)
0 - 14	22	3082	9216	12298	0.6
14 - 28	22	5031	15041	20071	0.6
28 - 42	22.5	4251	10051	14302	0.6
42 - 56	23	5072	9294	14365	0.6
56 - 70	23.5	5297	7432	12729	0.6
70 - 84	24	5935	5647	11582	0.6
84 - 98	24	4165	3957	8122	0.6
98 - 112	26	4021	891	4912	0.6
112 - 126	26	3946	868	4814	0.6
126 - 150	26.5	6459	1580	8039	1.0
150 - 200	26.5	9085	2180	11265	1.0
200 - 250	26.5	5975	1433	7409	1.0
250 - 300	26.5	4649	1116	5765	1.0
300 - 540	24	6028	11279	17308	1.2
540 - 900	24	1434	5498	6931	1.8



This figure "Lee.fig02.jpg" is available in "jpg" format from:

<http://arxiv.org/ps/astro-ph/0212252v1>

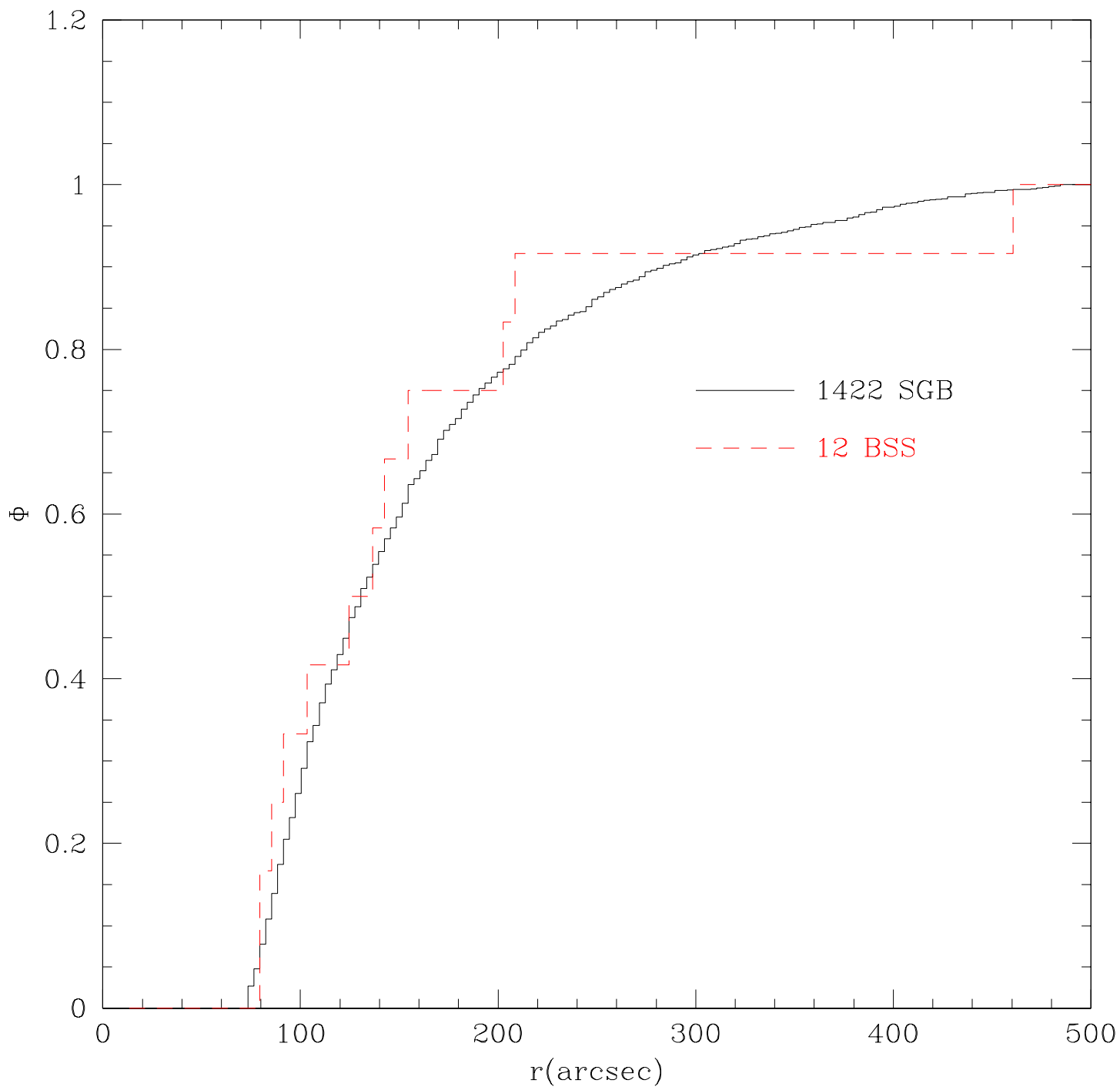


This figure "Lee.fig04.jpg" is available in "jpg" format from:

<http://arxiv.org/ps/astro-ph/0212252v1>

This figure "Lee.fig05.jpg" is available in "jpg" format from:

<http://arxiv.org/ps/astro-ph/0212252v1>



This figure "Lee.fig07.jpg" is available in "jpg" format from:

<http://arxiv.org/ps/astro-ph/0212252v1>

